
LIP-CAR: CONTRAST AGENT REDUCTION BY A DEEP LEARNED INVERSE PROBLEM

A PREPRINT

Davide Bianchi

School of Mathematics (Zhuhai),
Sun Yat-sen University,
Zhuhai, 519082, China.
bianchid@sysu.edu.cn.

Sonia Colombo Serra

Centro Ricerche Bracco,
Bracco Imaging SpA,
Colleretto Giacosa, 10010, Italy.
sonia.colombo@bracco.com.

Davide Evangelista

Department of Computer Science and Engineering,
University of Bologna,
Bologna, 40126, Italy.
davide.evangelista5@unibo.it

Pengpeng Luo

Bracco Imaging Medical Technologies Co. Ltd,
Shanghai, 200000, China.
ethe.luo@bracco.com.

Elena Morotti

Department of Political and Social Sciences,
University of Bologna,
Bologna, 40126, Italy.
elena.morotti4@unibo.it.

Giovanni Valbusa

Global R&D,
Bracco Imaging SpA,
Colleretto Giacosa, 10010, Italy.
giovanni.valbusa@bracco.com.

ABSTRACT

The adoption of contrast agents in medical imaging protocols is crucial for accurate and timely diagnosis. While highly effective and characterized by an excellent safety profile, the use of contrast agents has its limitation, including rare risk of allergic reactions, potential environmental impact and economic burdens on patients and healthcare systems. In this work, we address the contrast agent reduction (CAR) problem, which involves reducing the administered dosage of contrast agent while preserving the visual enhancement. The current literature on the CAR task is based on deep learning techniques within a fully image processing framework. These techniques digitally simulate high-dose images from images acquired with a low dose of contrast agent. We investigate the feasibility of a “learned inverse problem” (LIP) approach, as opposed to the end-to-end paradigm in the state-of-the-art literature.

Specifically, we learn the image-to-image operator that maps high-dose images to their corresponding low-dose counterparts, and we frame the CAR task as an inverse problem. We then solve this problem through a regularized optimization reformulation. Regularization methods are well-established mathematical techniques that offer robustness and explainability. Our approach combines these rigorous techniques with cutting-edge deep learning tools. Numerical experiments performed on pre-clinical medical images confirm the effectiveness of this strategy, showing improved stability and accuracy in the simulated high-dose images.

Keywords Deep Learning, Neural Networks, Inverse Problem Regularization, Contrast Agent, Computed Tomography, Magnetic Resonance Imaging, Iodine, Gadolinium, Explainability.

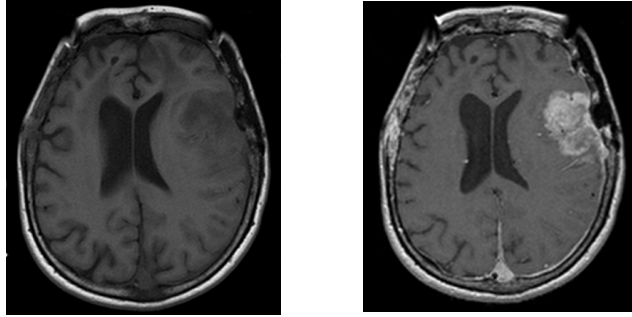


Figure 1: MRI images of a human brain [53], acquired without CA (on the left) and with a high dosage of CA (on the right).

1 Introduction

Modern technologies used for Computed Tomography (CT) and Magnetic Resonance Imaging (MRI) offer an unquestionable value to health care, but the visibility of very small or low-contrasted structures is not always guaranteed. Contrast Agents (CAs) are chemical compounds introduced into the patient’s body to alter the way the body interacts with physical stimuli (X-rays or magnetic fields) and, hence, to better distinguish (or “contrast”) lesions from healthy surrounding tissues. CAs are used in various diagnostic tasks, like searching for tumors [14, 58], mesenteric ischemia [34], pulmonary artery embolism [40], to cite just a few applications. See Figure 1.

Iodine- and gadolinium-based CAs are commonly employed in CT and MRI scans, respectively. These substances are generally deemed safe when administered within prescribed dose thresholds. Nevertheless, achieving a balance between administering a minimal amount of CA and obtaining high-fidelity imaging poses a notable challenge. For instance, despite rare or very rare, there are documented adverse effects associated with the use of these CAs [11, 49], and regulatory bodies like the European Medicines Agency have imposed restrictions on the use of certain linear gadolinium based CAs as a precaution about their retention/deposition in the brain and other tissues [1, 44], even if in the absence of any associated clinical sign.

In this scenario the scientific community is looking for solutions to reduce the use of CAs. In the following, we refer to the Contrast Agent Reduction (CAR) problem as the task of minimizing the level of CA while preserving the image enhancement granted by a high-level dose of CA.

Thanks to the recent advancements in deep learning, new purely digital imaging techniques have been developed to address the CAR problem. See for example [2, 9, 10, 22, 25, 28, 32, 36, 39, 41, 54]. In these works, deep neural network (NN) operators are used, taking an image (or a stack of images) acquired with a low dosage of CA and directly computing a simulation of the same image acquired with a high CA dosage. These approaches are learned “end-to-end” processing methods. In a compact way, we can write them as:

$$\Psi_{L2H}: \mathbf{x}_L \mapsto \mathbf{x}_H,$$

where Ψ_{L2H} is a pre-trained NN mapping low-dose to high-dose images, \mathbf{x}_L is the acquired low-dose image and \mathbf{x}_H is the desired high-dose image.

However, when dealing with real-world applications, every acquired image is contaminated by some unavoidable error of typically unknown distribution and sources. We take that into account by considering:

$$\mathbf{x}_L^\delta := \mathbf{x}_L + \boldsymbol{\eta}^{in}, \quad (1)$$

where \mathbf{x}_L represents the clean, inaccessible image and $\boldsymbol{\eta}^{in}$ is the intrinsic perturbation due to the (CT or MRI processing) imaging system. We reasonably assume $\|\boldsymbol{\eta}^{in}\|_2 \leq \delta$ with $\delta > 0$ and call δ the noise intensity. Under this notation, the learned end-to-end method takes the following final form:

$$\text{Given } \mathbf{x}_L^\delta, \quad \text{compute } \mathbf{x}_H^{\text{sim}} := \Psi_{L2H}(\mathbf{x}_L^\delta). \quad (2)$$

However, despite NNs achieving outstanding performance in end-to-end schemes for various imaging tasks, accuracy typically comes at the expense of robustness in deep learning. State-of-the-art literature has demonstrated that optimal

stability and accuracy cannot be achieved at the same time [3, 15, 24]. For instance, the network performance in end-to-end frameworks can be drastically affected by the presence of unquantifiable noise on the images when only a few noise intensities have been considered during the training phase [23]. This can cause artifacts to appear on the output image [20, 37], and even false positive details may arise [24]. Given the computational impracticality of training a NN across all potential noise intensities and distributions, or any generic perturbation, this presents a major challenge.

Additionally, the instability of deep-learning-based results is a significant concern in the medical field, which is one of the main areas involved in the Explainable-AI revolution [51]. This new discipline rejects the black-box nature of deep learning which prevents interpretation and thus undermines the reliability of medical practices. Instead, it promotes initiatives to advance data-based, mathematically- and technically-grounded medical applications of NNs. See [13, 26, 43, 45, 50] for some recent examples in this direction.

Due to all the aforementioned issues, we propose a paradigm shift. Instead of using a direct end-to-end approach, we look at the CAR problem as an inverse problem. We name our proposal LIP-CAR, referring to the Learned Inverse Problem for Contrast Agent Reduction, as illustrated in Figure 2. LIP-CAR operates in two primary stages.

Firstly, we train an image-to-image NN, denoted as Ψ_{H2L} , which is designed to map the acquired high-dose images to their (simulated) low-dose counterparts:

$$\Psi_{H2L} : \mathbf{x}_H \mapsto \mathbf{x}_L. \quad (3)$$

This NN operates inversely to Ψ_{L2H} , as illustrated in Figure 2. We denote the mapping function Ψ_{H2L} as the ‘‘LIP forward operator’’, as it represents the forward operation of our inverse problem, and it simulates the distribution of concentration of the chemical compound through the body by mapping high-dose to low-dose images.

Secondly, taking into account (1), we address the associated inverse problem:

$$\text{Given } \mathbf{x}_L^\delta, \text{ solve } \Psi_{H2L}(\mathbf{x}) = \mathbf{x}_L^\delta, \quad (4)$$

by means of regularized optimization techniques.

This shift in approach is crucial as it allows the use of a wide range of well-established and robust techniques from inverse problems regularization theory. On the one hand, we can stabilize the simulated high-dose images against perturbations in the low-dose acquired images; on the other hand, we can concentrate on enhancing the accuracy of the NNs with the confidence that, in the limit case, the simulated high-dose images converge to the true high-dose images.

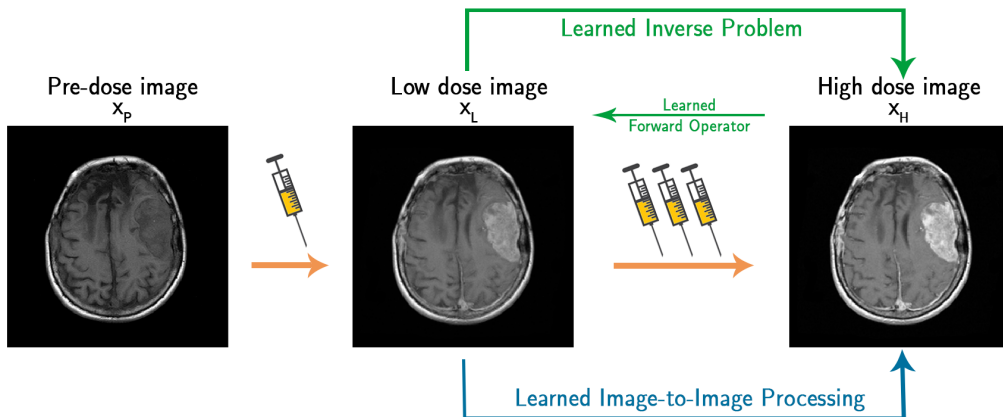


Figure 2: Visual representation of the paradigm change for the CAR task: from an end-to-end NN-based approach to a Learned Inverse Problem framework.

The contribution of this paper can thus be summarized as follows.

1. We introduce a new approach, LIP-CAR, for the CAR task that combines mathematical regularization techniques with cutting-edge deep learning tools in an accurate, well-performing two-step procedure. The convergence and stability of the method are guaranteed by a rigorous theoretical foundation.
2. LIP-CAR represents a versatile framework, realized here through distinct implementations. At the stage of formulating the inverse problem statement, we test two different regularizers to discuss the potential and

variety of regularization priors. Furthermore, the adaptability of the LIP forward operator easily allows for embedding registered pre-dose injection images, a known enhancer of data-driven performance.

3. Our numerical experiments, performed on a data set of pre-clinical images, assess that LIP-CAR can achieve high accuracy and is more robust than the end-to-end approach.

The manuscript is organized as follows: In Section 2 we briefly revise the state-of-the-art literature about the CAR problem. In Section 3 we introduce our new model method LIP-CAR along with a mathematical analysis of its regularization and stability properties. Sections 4-5 present the experimental setup and numerical results, respectively, where we compare the end-to-end method (2) and our regularized proposal (8). Finally, in Section 6 we draw the conclusions and outline future directions of research.

2 State of the art

Mathematical models for the CA distribution-excretion phenomenon have been introduced since the 1990s. We refer the reader to the seminal paper by Tofts et al. [52] and the references therein. However, on the one hand, the exact mechanism still remains unknown, and this is primarily due to the difficulty in fully understanding and accurately modeling the extensive range of complex physical and chemical interactions that occur within each different body following the administration of CAs. On the second hand, numerically solving the partial differential equations describing the phenomenon is challenging due to the ill-posed nature of the problem.

With the rise of deep learning, interest in the CAR problem as we intend it here and, more generally, in CA-related biomedical imaging problems, has seen a new surge in the scientific community. NNs are universal approximators [29], suggesting that with the correct architecture and training, the unknown CA distribution phenomenon can be well-approximated. In that sense recent results are promising. For example, in [46], the authors use Physics-Informed Neural Networks in combination with pharmacokinetic models to retrieve vascularization parameters in dynamic contrast-enhanced MRI. In [17], a novel neural network architecture is presented to quantify the concentration of superparamagnetic iron oxide particles, which are used as CAs in several MRI diagnostic tasks. In [56], an unsupervised method using the deep image prior technique is introduced for phase unwrapping in quantitative phase imaging, which is used for CA-free biomedical imaging. In [9], the authors train a V-Net to simulate high-dose MRI brain images from low-dose images acquired using only 25% of the standard gadolinium-based CA dose.

For the CAR problem, the state-of-the-art literature now strongly relies on NNs, and it always implements the direct end-to-end approach (2) by learning a Ψ_{L2H} operator. Notably, in papers such as [9, 10, 22, 25, 41], procedures with pre-dose image acquisition are considered and the authors have boosted the end-to-end operator defining it as:

$$\Psi_{PL2H} : (\mathbf{x}_P, \mathbf{x}_L) \mapsto \mathbf{x}_H. \quad (5)$$

In this case, both the pre-dose \mathbf{x}_P and low-dose images are passed as input to the NN to predict the high-dose one. This approach widely enhances the end-to-end performance, above all in terms of image accuracy.

However, one of the inherent challenges of the direct low-to-high approach lies within the task itself. We are transitioning directly from an image with smoother characteristics (low-dose) to one that exhibits more pronounced discontinuities (high-dose). As widely studied in the literature, this image enhancement process is not robust and prone to generate errors in case of even small inconsistencies on the data [27, 47]. Consequently, the end-to-end approach for CAR application may inherit ill-posedness from the underlying imaging task and its robustness with respect to perturbations (both in terms of extra noise and generalization error to unseen data) must be assessed. See, for example, [38], where false positives (artificial lesions) may appear in the digitally simulated high-dose images.

Interestingly, in many applications different than CA but still involving the digital processing of signals and images, the end-to-end usage of NNs is giving way to new hybrid approaches, where deep learning tools are embedded into variational schemes in a mathematically grounded scenario [21, 33]. In the vast available literature, in fact, deep networks have already been successfully used to learn optimal algorithmic parameters [4, 35], to define suitable regularizers [5–7, 12, 31, 48], or to speed up the reconstruction procedure [19]. All these studies have inspired us to design a novel use of NNs for the CAR problem.

3 The proposed method

We begin this section by establishing some of the notations and assumptions used throughout the remainder of the manuscript. We work on 2D slices with dimensions $H \times W$, although the framework is also applicable to 3D imaging with few adjustments. All images \mathbf{x} are grayscale and normalized to $[0, 1]$, for simplicity. They can be represented as functions $\mathbf{x} : P \rightarrow [0, 1]$, where $P = \{i \mid i = 1, \dots, n\}$ is the ordered set of pixels, and $n = H \cdot W$ is the fixed total

number of pixels. Thus, we can associate the space of images with the hypercube $[0, 1]^n := [0, 1] \times \dots \times [0, 1]$. In other words, for us, an image \mathbf{x} is an element of the hypercube $[0, 1]^n$,

$$\mathbf{x} = (\mathbf{x}(1), \dots, \mathbf{x}(n)) \in [0, 1]^n \subset \mathbb{R}^n.$$

We use the standard notation $\|\cdot\|_p$ for the ℓ^p -norms, $p \in [1, \infty]$. That is, $\|\mathbf{x}\|_p := (\sum_{i=1}^n |\mathbf{x}(i)|^p)^{1/p}$ for $p < \infty$ and $\|\mathbf{x}\|_\infty := \max_{i=1, \dots, n} |\mathbf{x}(i)|$ for $p = \infty$.

As previously introduced, we denote as \mathbf{x}_P , \mathbf{x}_L , and \mathbf{x}_H the pre-dose, low-dose, and high-dose images, respectively. The term ‘‘high-dose’’ denotes a standard reference level established either by a regulatory body or by laboratory protocols. Conversely, ‘‘low-dose’’ refers to instances where a reduced quantity of CA is administered to the patient, while ‘‘pre-dose’’ indicates the image acquired prior to any CA injections. These images can be acquired with a tomographic procedure or the MRI technique and then reconstructed as gray-scale images. We denote the digitally-simulated high-dose image as $\mathbf{x}_H^{\text{sim}}$, representing the target of the CAR imaging problem.

We can reasonably assume that the space of our images generated for a specific medical application belongs to a subset \mathcal{X} of the space of grayscale images, that is, $\mathcal{X} \subset [0, 1]^n$.

At last, we assume that there exists a natural phenomenon $\mathcal{F}: \mathcal{X} \rightarrow \mathcal{X}$ that decreases the CA concentration. However, this phenomenon is unknown or impossible to model precisely due to the large number of variables and hidden mechanisms involved.

3.1 NN operators for learning an inverse problem

From a mathematical point of view, a neural network Ψ is a chain of D compositions of affine transformations and possibly non-linear activation functions, and it can be compactly defined as:

$$\Psi(\mathbf{x}) := \sigma_D \left(W_D \left(\dots \left(\sigma_1 (W_1 \mathbf{x} + \mathbf{b}_1) \right) \dots \right) + \mathbf{b}_D \right)$$

where W_k and \mathbf{b}_k are matrices and bias vectors, respectively, defining the set of parameters $\{W_k, \mathbf{b}_k\}$, and σ_k are possibly non-linear functions. All modern architectures applied in image processing tasks generate continuous NN operators.

The overall combination of W_k , \mathbf{b}_k and σ_k , makes the architecture of a NN. The gist of a NN is that a subset $\Theta = \{W_{k'}, \mathbf{b}_{k'}\}$ of the parameter set is free and *trained* by minimizing a loss function \mathcal{L} over a collection of N input-output pairs $(\mathbf{x}_1^i, \mathbf{x}_2^i)_i$ for $i = 1, \dots, N$, that is:

$$\Theta_t = \underset{\Theta}{\operatorname{argmin}} \left\{ \sum_{i=1}^N \mathcal{L}(\Psi(\mathbf{x}_1^i), \mathbf{x}_2^i) \right\}. \quad (6)$$

Once the training phase is completed, Θ_t remains fixed, and so does Ψ . For a basic overview of NNs we refer to [8].

The widely used Ψ_{L2H} operators are trained using couples $(\mathbf{x}_L^i, \mathbf{x}_H^i)_i$ to learn the (pseudo) inverse \mathcal{F}^\dagger function.

Still exploiting NN operators, our method introduces a change of perspective from the paradigm in the state-of-the-art literature, as we aim to learn the \mathcal{F} phenomenon.

In fact, our first task is to find the operator $\Psi_{H2L}: \mathcal{X} \rightarrow \mathbb{R}_+^n$ introduced in Equation (3), transitioning from a signal with higher discontinuity (high-dose image) to a smoother one (low-dose image). It is expected to be more well-behaved and stable than Ψ_{L2H} .

To obtain it, we train Ψ_{H2L} using the available high-dose data as input \mathbf{x}_H^i images and the corresponding low-dose images as target \mathbf{x}_L^i , in the loss function (6). The trained operator thus generates a simulated low-dose image $\mathbf{x}_L^{\text{sim}}$, given the high-dose one:

$$\mathbf{x}_L^{\text{sim}} := \Psi_{H2L}(\mathbf{x}_H).$$

The Ψ_{H2L} network, mimicking \mathcal{F} , represents the LIP forward operator.

The presence of the forward operator allows the CAR reformulation as the inverse problem stated in (4). Indeed, our second task is the computation of the high-dose simulated image $\mathbf{x}_H^{\text{sim}}$, defined as a solution of the Ψ_{H2L} -associated inverse problem, i.e.:

$$\mathbf{x}_H^{\text{sim}} \quad \text{such that} \quad \Psi_{H2L}(\mathbf{x}_H^{\text{sim}}) = \mathbf{x}_L.$$

We remark that we also consider the LIP forward neural network Ψ_{PH2L} , defined as:

$$\Psi_{PH2L}: (\mathbf{x}_P, \mathbf{x}_H) \mapsto \mathbf{x}_L, \quad (7)$$

inspired by the operator in (5). It can be used in place of Ψ_{H2L} in Equation (4), when the no CA-enhanced signal \mathbf{x}_p is available. For the sake of clarity, we will henceforth omit explicit consideration of this case in the remainder of this section, as the associated modifications to the LIP-CAR framework are trivial in nature from the baseline model using the Ψ_{H2L} operator.

3.2 The regularized LIP-CAR model

It is known in the literature that solving an inverse problem through an optimization reformulation can offer advantages in terms of efficiency, flexibility, and robustness compared to direct inversion methods. Formally, we substitute the original operator Ψ_{H2L} with a family $\{\Psi_{\text{H2L},\alpha}\}_{\alpha \in \mathbb{R}_+}$ of stable operators $\Psi_{\text{H2L},\alpha}: \mathcal{X} \rightarrow \mathcal{Y} \supseteq \mathcal{X}$ such that point-wise converge to the (pseudo) inverse of Ψ_{H2L} , as α goes to zero. See for example [18].

We thus reformulate the LIP problem (4) with the regularized optimization problem:

$$\mathbf{x}_H^{\text{sim}} \in \underset{\mathbf{x} \in \mathcal{X}}{\operatorname{argmin}} \left\{ \frac{1}{2} \|\Psi_{\text{H2L}}(\mathbf{x}) - \mathbf{x}_L^\delta\|_2^2 + \alpha \mathcal{R}(\mathbf{x}) \right\} \quad (8)$$

which defines our LIP-CAR model. In this expression, the least square term forces the data fidelity of the simulated high-dose image, considering the presence of white intrinsic noise $\boldsymbol{\eta}^{\text{in}}$ (described in Equation (1)). The component $\mathcal{R}(\mathbf{x})$ serves as a regularization term, and the regularization parameter $\alpha > 0$ balances the trade-off between data fidelity and the regularization effect. The regularization operator \mathcal{R} is of crucial importance. In the limit (and unrealistic case), the perfect regularizer is given by:

$$\mathcal{R}(\mathbf{x}) := \begin{cases} 0 & \text{if } \mathbf{x} = \mathbf{x}_H, \\ +\infty & \text{otherwise.} \end{cases}$$

This suggests that, if we have access to a-priori information on the solution \mathbf{x}_H , we can tailor a specific \mathcal{R} to incorporate such information and penalize all the candidate solutions \mathbf{x} that do not present the features we aim to recover.

To set \mathcal{R} , we exploit the well-established regularization techniques that have already been extensively studied to offer a reliable approximation of a solution to the LIP inverse problem (4). This grants robustness and explainability to our approach, as we show in the Section 3.3.

For the sake of simplicity and to keep this paper self-contained, in the numerical experiments of Section 5, we focus on a generalized Tikhonov $\ell^2 - \mathcal{R}$ formulation. We consider the ℓ_1 -Total Variation (TV) norm:

$$\mathcal{R}(\mathbf{x}) = \|\nabla \mathbf{x}\|_1 \quad (9)$$

where ∇ denotes the gradient operator. The TV prior encourages sparsity in image gradients, which leads to sharper and more well-defined edges in the reconstructed images, improving the visual detection of medical details and aiding clinicians in identifying anatomical structures and abnormalities more accurately.

In order to exploit a-priori information, in Section 5 we also consider the Generalized ℓ_1 -Total Variation (GenTV) regularizer, which ensures that the solution image closely resembles a possibly good guess of $\mathbf{x}_H^{\text{sim}}$, in terms of gradient transforms. Denoting that guess as $\overline{\mathbf{x}}_H$, GenTV reads:

$$\mathcal{R}(\mathbf{x}) = \|\nabla(\mathbf{x} - \overline{\mathbf{x}}_H)\|_1. \quad (10)$$

In our scenario, GenTV can easily take advantage of the end-to-end networks, and $\overline{\mathbf{x}}_H$ can be computed as $\Psi_{\text{L2H}}(\mathbf{x}_L)$. We remark that our selection of the regularization function is merely illustrative, since the LIP-CAR approach lets us accommodate models other than (8) for regularizing the inverse problem.

At last, we highlight that the minimization problem (8) must be solved with an iterative procedure to be set according to the mathematical properties of the regularization function.

3.3 Convergence analysis of LIP-CAR

We now prove that our LIP-CAR model (8) is well-posed and convergent; that is, it admits solutions that continuously depend on the data and converge to the true high-dose image \mathbf{x}_H in the limit of infinite NN parameters and zero noise. In particular, this section explicitly shows the dependence of the LIP forward operator Ψ_{H2L} on the set Θ of trainable parameters introduced in Section 3.1. To make our analysis more general, we do not prescribe a fixed \mathcal{R} .

We enumerate the final output of each training phase by $\Theta_{t,k}$, indicating that $\Theta_{t,k}$ is the set of free parameters fixed at the end of the k -th training, $k \geq 1$, as briefly discussed in Section 3.1. Each training can differ from the others in

many ways, such as the number of input-output pairs, the optimizer, and the training hyperparameters, to name a few. We do not discuss these differences in-depth. Let us just note that, even if the overall architecture of the NN is fixed, the number of parameters is allowed to increase, that is, $\#\Theta_{t,k} \leq \#\Theta_{t,k+1}$. This increase reflects the idea that the depth of the NN (i.e. the number of layers) can be enhanced to achieve better accuracy.

For each $\Theta_{t,k}$, we have the corresponding trained LIP forward operator:

$$\Psi_{\text{H2L},k} : \mathcal{X} \rightarrow \mathbb{R}_+^n.$$

We need two batches of hypotheses. The first batch is as follows:

- (H1) The set of (medical) images \mathcal{X} is closed and regular;
- (H2) $\mathcal{F} : \mathcal{X} \rightarrow \mathcal{X}$ is bijective and continuous;
- (H3) $\sup_{\mathbf{x} \in \mathcal{X}} \|\Psi_{\text{H2L},k}(\mathbf{x}) - \mathcal{F}(\mathbf{x})\|_\infty \leq M_k \rightarrow 0$ as $k \rightarrow \infty$.

These hypotheses are very plausible. Hypothesis (H1) is technical, and it serves only to avoid unrealistic pathological cases in real-world applications. Regularity means that the boundary of \mathcal{X} is a set of zero Lebesgue measure, and it is safe to assume that every accumulation point of \mathcal{X} is still a medical image. Regarding (H2), the unknown operator \mathcal{F} is assumed to have an inverse, or a pseudo-inverse, \mathcal{F}^\dagger , which represents the anti-diffusion of the CA concentration and maps low-doses images to high-dose images. Moreover, we can assume that each of the n -th components of $\mathcal{F} = (\mathcal{F}_1, \dots, \mathcal{F}_n)$ are Lebesgue-measurable functions. Therefore, by Lusin-type theorems, it is possible to identify \mathcal{F} with a continuous function outside a set of arbitrarily small Lebesgue measures.

Regarding the third hypothesis (H3), we recall that NNs possess universal approximation properties; see [29] and especially [57, Theorem 1]. Thus, it is reasonable to assume that the sequence $\{\Psi_{\text{H2L},k}\}_{k \in \mathbb{N}}$ converges uniformly to \mathcal{F} , provided the right classes of architectures are chosen, and the training phases are sufficiently accurate.

We are in the position to begin our analysis.

Definition 1 (Solutions). *Given $\mathbf{x}_L \in \mathcal{X}$, we call \mathbf{x}_H the unique solution of:*

$$\mathcal{F}(\mathbf{x}) = \mathbf{x}_L.$$

An element $\mathbf{x}_k^\dagger \in \mathcal{X}$ is an \mathcal{R} -minimizing solution of the LIP problem (4), in the limit case $\delta = 0$, if $\Psi_{\text{H2L},k}(\mathbf{x}_k^\dagger) = \mathbf{x}_L$ and:

$$\mathcal{R}(\mathbf{x}_k^\dagger) = \min \{ \mathcal{R}(\mathbf{x}) \mid \mathbf{x} \in \mathcal{X}, \Psi_{\text{H2L},k}(\mathbf{x}) = \mathbf{x}_L \}.$$

We introduce now the second batch of hypotheses:

- (H4) $\Psi_{\text{H2L},k}$ is continuous for every k ;
- (H5) $\Psi_{\text{H2L},k}(\mathcal{X}) \supseteq \mathcal{F}(\mathcal{X})$;
- (H6) $\mathcal{R} : \mathcal{X} \rightarrow [0, +\infty)$ is continuous.

Notice that Hypothesis (H4) is verified for every NN architecture used in applications since all the activation functions in the inference phase are typically component-wise Lipschitz continuous. Hypothesis (H5) is instead a natural consequence of (H3).

In the next results, we provide well-posedness, stability, and convergence properties. The proofs are mostly standard, but for the convenience of the reader we highlight the key-points. We implicitly assume the validity of all the hypotheses (H1)-(H6) so far introduced.

Now, we define:

$$\begin{aligned} \Gamma_{k,i}(\mathbf{x}) &:= \frac{1}{2} \|\Psi_{\text{H2L},k}(\mathbf{x}) - \mathbf{x}_L^{\delta_{k,i}}\|_2^2 + \alpha_{k,i} \mathcal{R}(\mathbf{x}), \\ \Gamma_k(\mathbf{x}) &:= \frac{1}{2} \|\Psi_{\text{H2L},k}(\mathbf{x}) - \mathbf{x}_L^{\delta_k}\|_2^2 + \alpha_k \mathcal{R}(\mathbf{x}). \end{aligned}$$

Lemma 2 (Well-posedness). *For every $k \in \mathbb{N}$ there exists an \mathcal{R} -minimizing solution \mathbf{x}_k^\dagger , and the sets $\operatorname{argmin}_{\mathbf{x} \in \mathcal{X}} \{\Gamma_{k,i}(\mathbf{x})\}$ and $\operatorname{argmin}_{\mathbf{x} \in \mathcal{X}} \{\Gamma_k(\mathbf{x})\}$ are non-empty.*

Proof. The subset $S := \{\mathbf{x} \in \mathcal{X} \mid \Psi_{\text{H2L},k}(\mathbf{x}) = \mathbf{x}_L\}$ is non-empty and compact. Thus, $\mathcal{R}|_S$ admits a minimizer.

In the same way, by continuity and compactness, $\Gamma_{k,i}$ and Γ_k achieve a minimum on \mathcal{X} . \square

Theorem 3 (Stability). *Set a sequence $\delta_{k,i}$ of noise intensities such that $\lim_i \delta_{k,i} = \delta_k > 0$ for every k , and fix $\alpha_{k,i} = \alpha_k > 0$ for every i .*

Then any sequence $\{\mathbf{x}_{H,k,i}^{\text{sim}}\}_{i \in \mathbb{N}}$ of elements $\mathbf{x}_{H,k,i}^{\text{sim}} \in \underset{\mathbf{x} \in \mathcal{X}}{\text{argmin}}\{\Gamma_{k,i}(\mathbf{x})\}$ has a convergent subsequence such that:

$$\lim_{i'} \mathbf{x}_{H,k,i'}^{\text{sim}} = \mathbf{x}_{H,k}^{\text{sim}} \in \underset{\mathbf{x} \in \mathcal{X}}{\text{argmin}}\{\Gamma_k(\mathbf{x})\}.$$

If $\mathbf{x}_{H,k}^{\text{sim}}$ is unique, then the whole sequence $\mathbf{x}_{H,k,i}^{\text{sim}}$ converges to $\mathbf{x}_{H,k}^{\text{sim}}$.

Proof. By Lemma 2, the sequence $\{\mathbf{x}_{H,k,i}^{\text{sim}}\}_{i \in \mathbb{N}}$ is well-posed. By compactness there exists a convergent subsequence $\lim_{i'} \mathbf{x}_{H,k,i'}^{\text{sim}} = \mathbf{x}_{H,k}^{\text{sim}}$. By continuity and the definition of $\mathbf{x}_{H,k,i}^{\text{sim}}$,

$$\Gamma_k(\mathbf{x}_{H,k}^{\text{sim}}) = \lim_{i'} \Gamma_{k,i'}(\mathbf{x}_{H,k,i'}^{\text{sim}}) \leq \lim_{i'} \Gamma_{k,i'}(\mathbf{x}) = \Gamma_k(\mathbf{x})$$

for any $\mathbf{x} \in \mathcal{X}$. Thus, $\mathbf{x}_{H,k}^{\text{sim}} \in \underset{\mathbf{x} \in \mathcal{X}}{\text{argmin}}\{\Gamma_k(\mathbf{x})\}$. If $\mathbf{x}_{H,k}^{\text{sim}}$ is unique, then every subsequence of $\{\mathbf{x}_{H,k,i}^{\text{sim}}\}_{i \in \mathbb{N}}$ has a convergent sub-subsequence to $\mathbf{x}_{H,k}^{\text{sim}}$. By a standard topological argument, $\lim_i \mathbf{x}_{H,k,i}^{\text{sim}} = \mathbf{x}_{H,k}^{\text{sim}}$. \square

Theorem 4 (Convergence). *Let $\mathbf{x}_L \in \mathcal{X}$ be fixed and \mathbf{x}_H be the unique solution of $\mathcal{F}(\mathbf{x}) = \mathbf{x}_L$. Let $\{\delta_{k,i}\}_{k,i \in \mathbb{N}}$ be any sequence of strictly positive noise intensities such that $\lim_i \delta_{k,i} = 0$ for every k . Chose $\alpha_{k,i}: (0, +\infty) \rightarrow (0, +\infty)$ such that $\lim_i \alpha_{k,i} = 0$ and $\lim_i \delta_{k,i}^2 / \alpha_{k,i} = 0$ for every k .*

Then any sequence of elements $\mathbf{x}_{H,k,i}^{\text{sim}} \in \underset{\mathbf{x} \in \mathcal{X}}{\text{argmin}}\{\Gamma_{k,i}(\mathbf{x})\}$ admits a subsequence such that $\lim_{i'} \mathbf{x}_{H,k,i'}^{\text{sim}} = \mathbf{x}_k^\dagger$. If \mathbf{x}_k^\dagger is unique, then $\lim_i \mathbf{x}_{H,k,i}^{\text{sim}} = \mathbf{x}_k^\dagger$. Moreover, if $\lim_k \delta_{k,k} = \lim_k \alpha_{k,k} = 0$, then $\lim_k \mathbf{x}_{H,k,k}^{\text{sim}} = \mathbf{x}_H$.

Proof. The first part is a straightforward application of standard techniques. See for example the proof in [47, Theorem 3.26]. For every k , fix now an \mathcal{R} -minimizing solution \mathbf{x}_k^\dagger . Then,

$$\Gamma_{k,k}(\mathbf{x}_{H,k,k}^{\text{sim}}) \leq \Gamma_{k,k}(\mathbf{x}_k^\dagger) \leq \delta_{k,k}^2 + \alpha_{k,k} \mathcal{R}(\mathbf{x}_k^\dagger).$$

By passing to a subsequence, if necessary, we have that $\lim_{k'} \mathbf{x}_{H,k',k'}^{\text{sim}} = \mathbf{x}^*$ and $\lim_{k'} \mathbf{x}_k^\dagger = \mathbf{x}^{**}$, with $\mathbf{x}^*, \mathbf{x}^{**} \in \mathcal{X}$. Therefore:

$$\lim_{k'} \Gamma_{k',k'}(\mathbf{x}_{H,k',k'}^{\text{sim}}) = 0,$$

and it follows that:

$$\lim_{k'} \|\Psi_{\text{H2L},k'}(\mathbf{x}_{H,k',k'}^{\text{sim}}) - \mathbf{x}_L^{\delta_{k',k'}}\|_2 = 0.$$

Using now the uniform convergence (H3), we get:

$$\mathbf{x}_L = \lim_{k'} \Psi_{\text{H2L},k'}(\mathbf{x}_{H,k',k'}^{\text{sim}}) = \mathcal{F}(\mathbf{x}^*),$$

that is, $\mathbf{x}^* = \mathbf{x}_H$. Since \mathbf{x}_H is unique, by a standard topological argument, $\lim_k \mathbf{x}_{H,k,k}^{\text{sim}} = \mathbf{x}_H$. \square

3.4 Robustness and stability of LIP-CAR

While powerful tools, NNs are typically susceptible to errors and vulnerabilities. They learn to mimic the behavior of an operator through a statistical optimization process over a finite training set, but they must demonstrate efficiency and accuracy when presented with test data and unseen input. This property is typically referred to as ‘‘robustness’’. It ensures that the network has effectively learned existing patterns rather than merely memorizing the training data. Therefore, evaluating our networks’ performance on unseen data is crucial for assessing the true effectiveness of our proposed approach and its reliability for practical applications in CA imaging.

More precisely, referring to the wide literature about NN robustness, the ‘‘generalization error’’ for a trained network is typically defined as the difference between the performance of the network on the training data and its performance on unseen data from the same distribution. It quantifies how well the network can generalize its learned patterns to new, consistent examples (composing the so-called ‘‘in-domain’’ test set). Experiments reported in Section 5 will analyze the generalization ability of all the considered learned operators, by comparing their performance of training and testing data.

In addition, since the seminal paper [23] by Goodfellow et al., adversarial examples, crafted to deceive neural networks by making imperceptible or small changes to input data, have been used to highlight the vulnerability of neural networks on slightly inconsistent data. As anticipated in Section 1, the presence of noise is unavoidable in medical applications, but intrinsic components as in (1) are assumed to share similar properties over the entire data set, built under the same medical protocol. However, the presence of extra noise in a few patients’ images represents a particularly significant and plausible perturbation that must be considered. An elevated noise level may result from many factors, including calibration issues or patient anomalies. In these cases, the unexpected perturbation is called “out-of-domain” noise, as it represents a statistically significant mismatch between training and test samples that can cause severe artifacts or even hallucinations on some output images.

Recalling numerical analysis classical theory, from now on, we call “stability” the robustness of an NN-based approach with respect to out-of-domain noise.

Remark 5. Theorem 3 in Section 3.3 has already theoretically stated that, for every k , the model (8) is continuous and stable against extra perturbations $\delta_{k,i} = \delta_k \pm \delta_i \neq \delta_k$. In Section 5.3, we will assess the stability of the LIP-CAR approach numerically. These analyses are important when handling NNs since their performances can be heavily affected by generalization errors stemming from unseen data and types of perturbations different from the ones present in the training set. Assuming moreover that \mathcal{R} is convex, it is possible to control the rate of convergence of $\mathbf{x}_{H,k,i}^{\text{sim}}$ towards \mathbf{x}_k^\dagger using the Bregman distance $D_\xi^{\mathcal{R}}(\cdot, \cdot)$, induced by \mathcal{R} in a fixed direction ξ , such that

$$D_\xi^{\mathcal{R}}(\mathbf{x}_{H,k,i}^{\text{sim}}, \mathbf{x}_k^\dagger) \approx \delta_{k,i}.$$

The proof is technical, so we omit it here. Interested readers can refer to [47, Theorem 3.42] for details. The key point is that the regularization term \mathcal{R} controls and smooths out the perturbations in $\mathbf{x}_{H,k,i}^{\text{sim}}$ caused by the extra noise $\delta_{k,i}$. This presents another notable difference compared to the direct end-to-end method (2).

4 Experimental setup

In this section we illustrate our experimental design, by describing the CA data set and our methodological and implementation choices, before analysing the numerical results in Section 5.

4.1 Data set

We conduct our study on real contrast agent images from a pre-clinical trial. Procedures were conducted according to the national and international laws on experimental animal research (L.D. 26/2014; Directive 2010/63/EU) and under a specific Italian Ministerial Authorization (project research number 215/2020-PR), by CRB/Test Facility of Bracco Imaging SpA. The original dataset is composed of 61 cranial MRI examinations of lab rats affected by an orthotopically induced C6 glioma. Specifically, each lab rat underwent an MRI session composed of three T1-weighted spin echo sequences (TR = 360 ms, TE = 5.51 ms, echo spacing = 5.514 ms, rare factor = 2, FOV = 32 mm x 32 mm, matrix size = 256 x 256, number of slice = 24, slice thickness 0.75 mm, number of averages = 4) respectively acquired before any administration (pre- CA), after administration of 0.01 mmol Gd/kg of a non-commercial high relaxivity dimeric gadolinium based CA (low-dose image), and after administration of additional 0.04 mmol Gd/kg of the same agent (a full-dose image).

Having MRI 3D data as stacks of 24 slices, we split the volumes into 2D images of 256x256 pixels. After cleaning the data set by removing slices with missing or poorly registered sequences, we randomly split the data into training and testing subsets. We consider $N = 840$ images for training and $N = 240$ images for testing.

The presence of unavoidable intrinsic noise η^{in} on all the images made us consider pre-processing the data with a denoising tool before proceeding with training procedures. However, our analysis of noise statistics indicated that the high-dose images exhibited small perturbations on average, and we found it was not worth risking the loss of details and contrast reduction on the high-dose images. On the contrary, the low-dose slices were more significantly impacted by noise and the benefits of their denoising are reported and discussed in Section 5.1. In these tests, we opted for the BM3D filter [16], which is a block-matching and filtering method for denoising, and it represents a state-of-the-art tool that has been shown to be very effective in removing noise from images.

4.2 Approaches and notations

As mentioned, the proposed LIP-CAR approach has a flexible design. For instance, we have considered both the LIP forward operators introduced in section 3.1, i.e. Ψ_{L2H} defined in Equation (3) and Ψ_{PL2H} defined in Equation (7). We have also exploited the modularity of the optimization problem statement and considered both the TV prior as in Equation (9) and the GenTV regularizer defined in Equation (10).

We focus on the following three main learned inverse problems in the numerical experiments.

We denote as **LIP-H2L-TV** and **LIP-PH2L-TV** the cases where the Total Variation regularizer is considered and the forward operator is played by the Ψ_{H2L} or Ψ_{PH2L} networks, respectively. We remark that the LIP-H2L-TV solver does not consider pre-dose images at all, hence it may be of interest for those cases where registered pre-dose and low-dose images are not available.

Then, the label **LIP-PH2L-GenTV** refers to the inverse problem solver where the forward operator is played by Ψ_{PH2L} and the Generalized Total Variation regularizer is considered. In this case, GenTV relies on the $\overline{x_{\text{H}}}$ image computed by the Ψ_{PL2H} operator. We observe that this implementation heavily exploits all the provided items and tools at best, by using the pre-dose images for training the LIP forward operator and using the images by the end-to-end approach inside the regularization term.

Both the LIP forward operators and LIP-CAR framework are compared to the state-of-the-art, i.e. the trained networks Ψ_{L2H} and Ψ_{PL2H} . In the next section, where we compare all the computed $x_{\text{H}}^{\text{sim}}$ images, we will use the notations **NN-L2H** and **NN-PL2H** to emphasize their reliance on the NN direct application (2), in contrast to the LIP formulation.

4.3 Metrics for quality assessment

To quantify the performance of the considered approaches, we consider three quality assessment metrics:

1. Relative Error:

$$\text{RE}(\mathbf{x}_1, \mathbf{x}_2) := \frac{\|\mathbf{x}_1 - \mathbf{x}_2\|_2}{\|\mathbf{x}_2\|_2}.$$

As the RE computes the ℓ_2 distance between two images, the lower the RE, the better the performance of the NN.

2. Structural Similarity Index Measure (SSIM): The $\text{SSIM}(\mathbf{x}_1, \mathbf{x}_2)$ has been defined in [55] to quantify the similarity of the \mathbf{x}_1 image with respect to the reference \mathbf{x}_2 image, capturing visual elements. The closer the SSIM is to 1, the better the performance of the NN.
3. Peak Signal-to-Noise Ratio:

$$\text{PSNR}(\mathbf{x}_1, \mathbf{x}_2) := 20 \log_{10} \left(\frac{\max_i |\mathbf{x}_2(i)|}{\|\mathbf{x}_1 - \mathbf{x}_2\|_2} \right).$$

The higher the PSNR, the better the performance of the NN.

In addition to the assessment metrics, we will present images to examine the differences among methods and visually compare the contrast enhancements introduced onto the images.

4.4 Network architecture and training

To lead fair comparisons, we always use the deep architecture considered in [9] and in [2], thus representing the state-of-the-art for the CAR imaging task. In these manuscripts, the authors address the low-dose contrast agent problem with a variant of the U-net architecture, firstly introduced in [42] for bio-medical image segmentation, commonly referred to as V-Net. The reference architecture is thus a multiscale convolutional neural network, with strided convolutions instead of maxpooling layers for downsampling. Our V-Net architecture has few differences from the original one, due to the different structure of the considered dataset. First of all, we consider an input layer with just low-dose/high-dose images, stacked with pre-dose images when available, differently to the original manuscript implementation [9], where the inputs were the concatenation of pre-dose, low-dose, T2-Flair, and diffusion images. Secondly, we modified the final sigmoid activation function with a ReLU to address stability issues in the training phase.

When specified, the input low-dose images are substituted with their corresponding BM3D-filtered version.

In all our experiments, the NNs are trained for 80 epochs and batch size of 16, with the Adam optimization algorithm [30] and fixed step size of 10^{-3} . They are trained to minimize the mean of the SSIM-based loss function $\text{SSIM}(\cdot, \cdot)$ over the set of trainable parameters Θ :

$$\text{argmin}_{\Theta} \frac{1}{N} \sum_{i=1}^N (1 - \text{SSIM}(\Psi(\mathbf{x}_1^i), \mathbf{x}_2^i)), \quad (11)$$

where Ψ is a generic NN with trainable parameters set Θ , N is the number of training data, \mathbf{x}_1^i are the inputs of the network and \mathbf{x}_2^i the target images.

All the training procedures were executed on an NVIDIA Quadro P6000 GPU card, requiring approximately 20 minutes for the whole training process.

4.5 Specifications about the regularized model

To solve the regularized inverse problem, we have exploited the widely used Adam solver. We have always used the low-dose image as a starting iterate and run 150 iterations.

The regularization parameters α used in (8) have been chosen heuristically to better balance the visual appearance of the output and their metrics. For the LIP-H2L-TV model, we have used $\alpha = 6e - 3$, for the LIP-PH2L-TV $\alpha = 3e - 3$ while for the LIP-PH2L-GenTV $\alpha = 6e - 3$.

To analyze the stability of the LIP-CAR approach in case of out-of-domain noise, we will alter the low-dose input image of the test set by adding a random perturbation η^{out} drawn from a Gaussian white distribution with fixed noise level. The corrupted test data thus reads:

$$\mathbf{x}_L^\delta + \eta^{out}. \quad (12)$$

In section 5.3 we consider several noise realizations with increasing intensities, up to 0.066 standard deviation. Due to the high perturbation, the regularization parameter α has been changed based on a logarithmic-spaced distribution in the interval $[3e - 3, 0.01]$ for LIP-PH2L-TV approach, $[6e - 3, 0.01]$ for the LIP-H2L-TV and LIP-PH2L-GenTV models. The networks are not re-trained.

5 Numerical experiments

In this section, we first compare the trained networks used as image-to-image operators, focusing on their accuracy performances and on their generalization ability. Then we evaluate the proposed LIP-CAR approach on the in-domain test set in Section 5.2 and analyze its stability with respect to extra out-of-domain noise in Section 5.3.

5.1 Ablation study of image-to-image approaches

Here, we evaluate the performance of the NNs used as direct predictors, and we test the usefulness of the BM3D applied to the low-dose images. In Table 1, we report the mean and the standard deviation of the PSNR and SSIM values computed over the entire test set. Recalling the definitions provided in Section 4.3, we highlight that the target image of the first four rows is the high-dose image, hence we have used $\mathbf{x}_1 = \Psi(\mathbf{x}_L)$ and $\mathbf{x}_2 = \mathbf{x}_H$ (with the suitably trained networks Ψ). Conversely, in the last rows, we have set $\mathbf{x}_1 = \Psi(\mathbf{x}_H)$ and $\mathbf{x}_2 = \mathbf{x}_L$.

NN	preprocessing on \mathbf{x}_L^δ	PSNR	SSIM
Ψ_{L2H}	None	28.14 (0.833)	0.855 (0.021)
	BM3D	28.79 (0.928)	0.859 (0.022)
Ψ_{PL2H}	None	28.89 (0.851)	0.868 (0.022)
	BM3D	29.34 (0.907)	0.866 (0.022)
Ψ_{H2L}	None	31.92 (1.110)	0.851 (0.025)
	BM3D	30.50 (0.939)	0.854 (0.026)
Ψ_{PH2L}	None	37.85 (0.885)	0.919 (0.007)
	BM3D	39.05 (1.073)	0.952 (0.007)

Table 1: Performance comparison of the image-to-image operators. We report the metrics’ mean and standard deviation (in brackets) on the full test set. We highlight in bold the operators used in the following experiments.

Looking at Table 1, firstly, we observe that we always get high SSIM values, reflecting the capability of all the considered image-to-image operators to approach their targets. The very small standard deviation values further confirm this.

Secondly, we appreciate the benefits of the use of the pre-dose images, making the low-to-high approach increase of one percentage point in SSIM and the high-to-low one increase up to 10 points (0.952 of SSIM from 0.854) while strongly reducing the standard deviation (only 0.007 from 0.025). Using \mathbf{x}_P images also helps mitigate noise on the

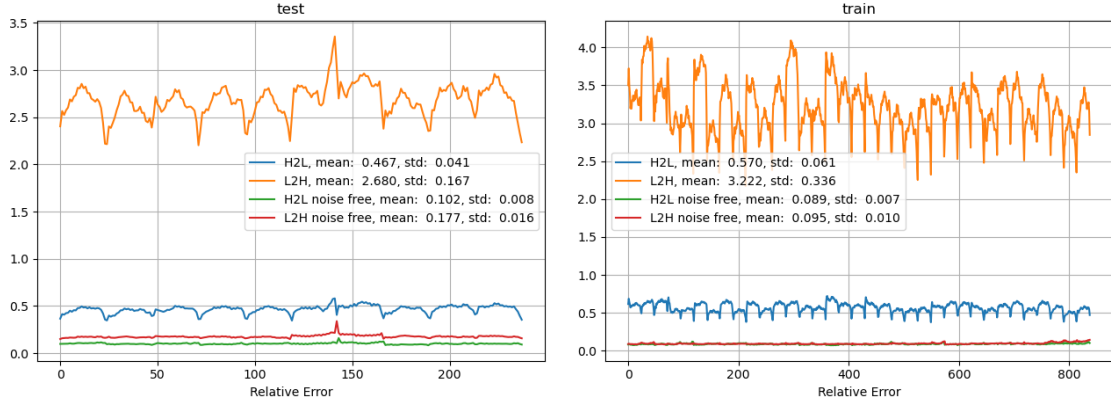


Figure 3: Values of relative errors computed on each image of the test set (left) and train set (right), in case of in-domain input images and in case of out-of-domain noisy input images.

outputs, as the PSNR values increase in all the reported cases, up to 39.05 for the Ψ_{PH2L} operator.

Thirdly, we highlight that learning the low-dose images produces the highest metrics, above all in terms of PSNR and independently on the use of the BM3D denoiser. This suggests that the LIP forward operators are simpler to learn than the end-to-end ones, as we had used very comparable training set-ups.

Lastly, we observe that using the BM3D to denoise the x_L images has mainly improved the Ψ_{PH2L} performance, whose PSNR gains more than one point and reaches its highest value. In the following, we will always consider the Ψ_{H2L} and Ψ_{PH2L} operators trained on denoised low-dose images, while we do not contemplate the BM3D anymore for Ψ_{L2H} and Ψ_{PL2H} .

We need to check the robustness of the end-to-end and the LIP forward operators now.

As discussed in Section 3.4, the network’s capability to generalize from training data is an important factor to assess. To estimate the generalization error due to the inherent differences between the statistical distribution of the training set (the only one considered for fine-tuning the learned parameters) and that of the test set, we carefully compare networks’ performances on the two sets. In the top image of Figure 3, we plot the RE values across all the 240 test images, and in the bottom image, those across the 840 train images. Table 2 reports the corresponding mean and standard deviation values to quantify the different behaviors through averages. We first focus on the in-domain cases, i.e., the actually acquired real data. As visible, the overall trend does not change remarkably: the errors are always small, and those on the test data are only slightly higher than those on the training samples (above all for Ψ_{PH2L} operator). In addition, there are extremely low variations from the means. We can conclude that the networks have not overfitted the training samples.

We also need to analyze the networks’ stability with respect to additive out-of-domain noise η^{out} , so we now apply the pre-trained Ψ_{PH2L} and Ψ_{PL2H} operators onto input images corrupted by further Gaussian noise with standard deviation $\sigma = 0.1$. We have replicated the in-domain performance analysis on both sets, and the results are still in Figure 3 and Table 2. As expected, the errors of the out-of-domain images are higher than the corresponding in-domain ones. However, if the Ψ_{PH2L} approach (in red) still exhibits values around 0.5 with moderate fluctuations when applied on strongly noisy images, Ψ_{PL2H} (in green) presents higher values with wide oscillations. This empirically demonstrates the instability of the low-to-high approach and the superiority of the LIP forward operator for the considered added noise.

	NN	in-domain	out-of-domain
test set	Ψ_{PL2H}	0.177 (0.016)	2.680 (0.167)
	Ψ_{PH2L}	0.102 (0.008)	0.467 (0.041)
train set	Ψ_{PL2H}	0.095 (0.010)	3.222 (0.336)
	Ψ_{PH2L}	0.089 (0.007)	0.570 (0.061)

Table 2: Mean and standard deviation (in brackets) of the relative errors computed on each image of the test and train sets, in case of in-domain input images and in case of out-of-domain noisy input images.

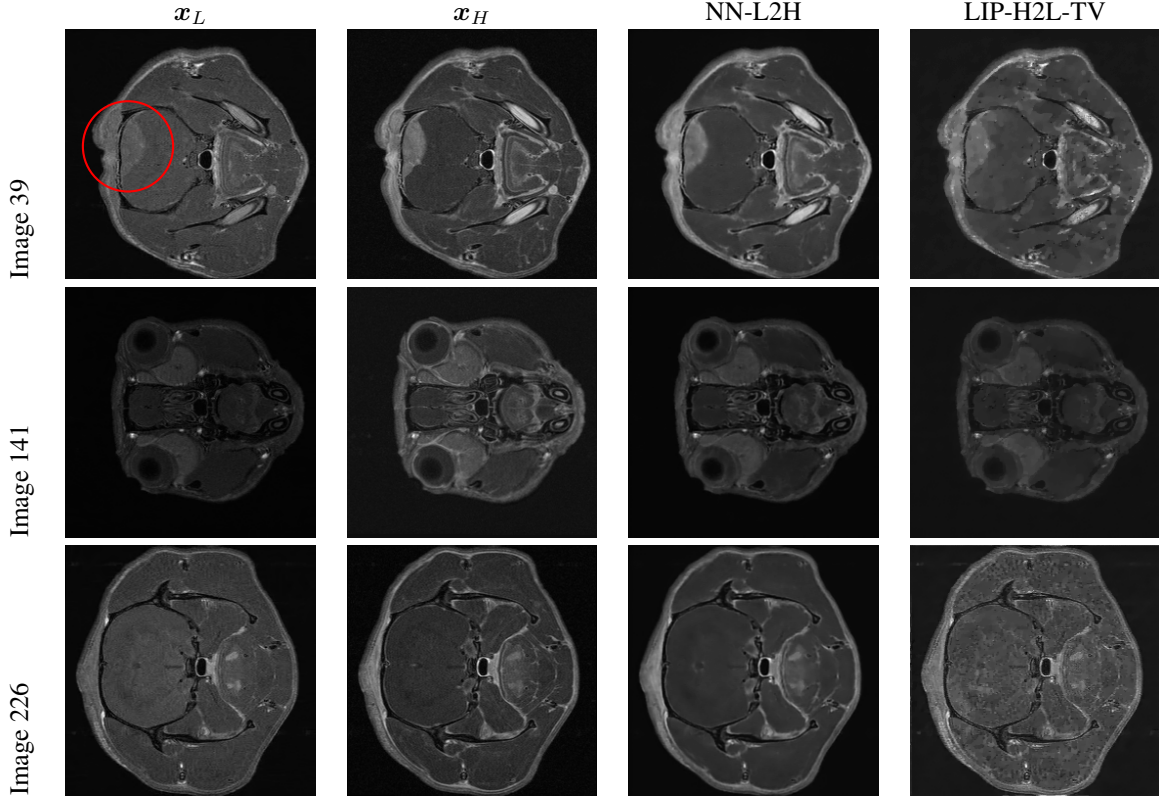


Figure 4: Results on test images number 39, 141 and 226, achieved from the low-dose x_L images (first column) having the high-dose x_H images (second column) as references: the NN-L2H framework based on the end-to-end Φ_{L2H} operator (third column), the LIP-H2L-TV proposed method based on the forward Φ_{PH2L} operator and the TV prior (9) (last column).

5.2 Accuracy of the LIP-CAR approach

Now, we test the proposed LIP-CAR framework and compare its high-dose simulated images to the end-to-end generated ones. Here, we consider only the in-domain case, and we postpone the robustness analysis to Section 5.3.

We start taking into consideration some reference test images in Figures 4 and 5. Specifically, test image 39 depicts a slice with a large glioma; image 226 shares a similar shapes but does not contain a tumoral mass of interest, whereas image 141 shows a completely diverse head morphology including the olfactory bulb and the eyes of the mouse.

In Figure 4, we illustrate the basic scenario where only the x_L and the x_H data are available for training: in this case, only the NN-L2H and the LIP-H2L-TV methods are usable to simulate high-dose images. We immediately observe that both approaches are able to detect all the areas that need to be enhanced/de-enhanced, without adding any false enhancements/de-enhancements (potentially causing hallucinations and false diagnosis). However, the LIP-CAR solutions are slightly noisy in the background and darker than the images by NN-L2H.

In Figure 5, we assume the pre-dose injection images x_P are available, and we can add them as input data for the training. As visible, the pre-dose image 39 is very noisy and its tumoral mass is not evident, while it is perfectly enhanced with neat boundaries in all the simulated high-dose images. In addition, all the computed images are well denoised, and they recovered fine details that were visible only in the corresponding high-dose slices (see, for instance, image 141). This visual inspection suggests that the addition of the pre-dose images strongly improves the contrast among relevant anatomical areas and, again, no false positives are added.

Focusing on the regularizers used in the LIP approach (third and fourth columns in Figure 5), we observe that the TV prior tends to smooth the reconstructions, while GenTV has remarkably taken advantage of the Ψ_{PH2L} operator, as its images are bright well contrasted. However, our LIP approach overcomes NN-PL2H firmly, in terms of metrics. Table 3 reports the SSIM values with respect to the high-dose target, for the pre-dose, the low-dose and all the simulated high-dose images. The values confirm that we always obtain reliable approximations of the reference high-dose images, as the starting SSIM values of the low-dose images increase remarkably, even with the naive LIP-H2L-TV approach. In

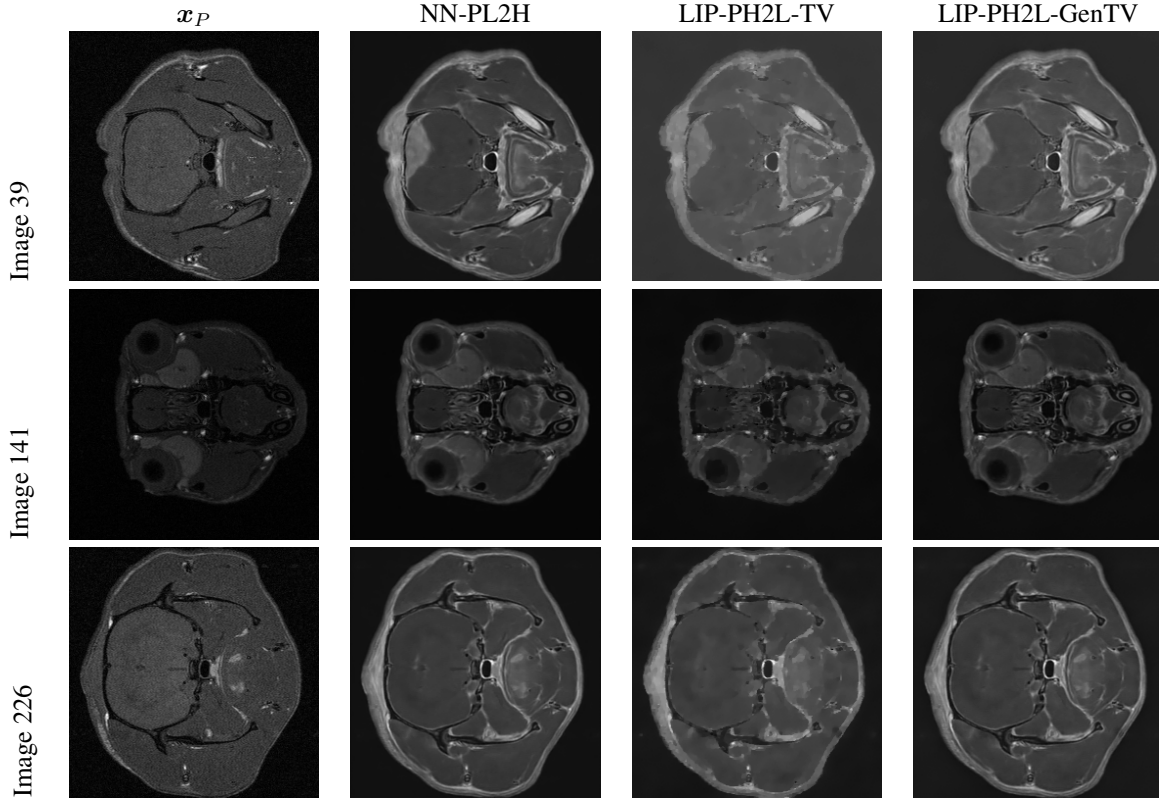


Figure 5: Results on test images number 39, 141 and 226, achieved when the pre-dose x_P images (first column) are available: the NN-PL2H framework based on the end-to-end Φ_{PL2H} operator (second column), the LIP-PH2L-TV proposed method based on the forward Φ_{PH2L} operator and the TV prior (9) (third column), and the LIP-PH2L-GenTV proposed method based on the Φ_{PH2L} operator and the GenTV prior (10) (last column).

some cases, the values of the NN approaches are slightly higher than the TV-based LIP approaches, but they do not achieve the highest metrics, which were always hit by LIP-PH2L-GenTV.

Approach	SSIM values		
	39th image	141th image	226th image
pre-dose	0.4118	0.3697	0.4512
low-dose	0.6627	0.6330	0.6821
NN-L2H	0.8646	0.8346	0.8680
NN-PL2H	0.8756	0.8488	0.8804
LIP-H2L-TV	0.8213	0.8376	0.8288
LIP-PH2L-TV	0.8713	0.8760	0.8690
LIP-PH2L-GenTV	0.9007	0.8883	0.9020

Table 3: SSIM values of the images reconstructed by the selected approaches, starting from the low-dose image, for three test images.

For a further visual inspection, in Figure 6, we show results on several test images depicting different elements of the mice heads. Here, we can further appreciate the capability of the NN-PL2H and LIP-PH2L-GenTV frameworks to always approximate the high-dose images carefully. In these images, the contrast of tumoral masses has been increased (see red circles), and meanwhile, no false positives have been generated in slices with no tumors, neither artifacts nor hallucinations. We conclude by noting that the LIP-PH2L-GenTV images are similar to the NN-PL2H

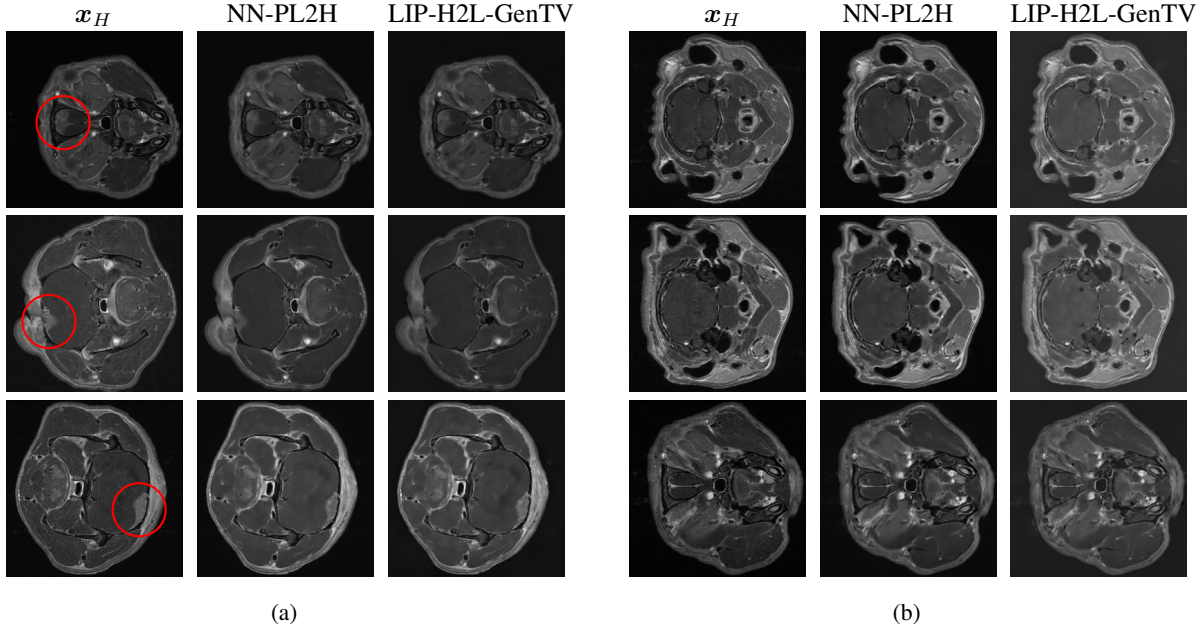


Figure 6: Results achieved on further test images, exploiting the pre-dose images. (a) Cases containing tumors, highlighted with red circles on the high-dose images; (b) cases containing no tumors.

ones at visual inspection but have better metrics. Therefore, our mathematically-grounded approach is competitive with the state-of-the-art.

5.3 Stability of the LIP-CAR approach with respect to noise

We now compare the methods on test images affected by additive η^{out} noise. We start considering the test image 39. We consider various noise intensities, given by standard deviation σ , and we report here the results for equispaced σ values in the $[0, 0.066]$ range. In Figure 7a, we plot the behavior of the SSIM values with respect to σ , for three LIP solvers and the state-of-the-art methods. When the additive noise is absent ($\sigma = 0$) or very small ($\sigma = 0.11$), the methods using the pre-dose images provide very high SSIM, strongly overcoming the LIP-H2L-TV method. The NN-L2H approach gives a medium-high quality solution as well. In the case of higher perturbations (right-hand side of the plot), there is a trend reversal where the NN-L2H, NN-PL2H, and LIP-PH2L-GenTV produce increasingly poor high-dose simulations as sigma increases. The GenTV constraint, which forces LIP-PH2L-GenTV “to remain close” to the NN-PL2H image, is negatively influenced by the instability of the NN-PL2H approach, as already observed in Section 5.1. The regularization of the inverse problem formulation only partially mitigates this effect, as LIP-PH2L-GenTV consistently maintains higher SSIM values than NN-PL2H. Interestingly, the two TV-regularized approaches remain stable and reliable in high out-of-domain noise, always providing SSIM values higher than 0.7.

For a broader comparison between the in- and the out-of-domain cases, we consider the SSIM values computed on the whole test set for $\sigma = 0$ and $\sigma = 0.033$. The corresponding boxplots are shown in Figure 7b. The median values are mostly coherent with the values depicted in Figure 7a about the 39th image, and it demonstrates that we did not cherry-pick that image. We also observe that the amplitudes of the boxplots are always very small, in the case of $\sigma = 0$, and a few outliers occurred. Conversely, when $\sigma = 0.033$, only our TV-based LIP approaches show limited boxplots with short whiskers, while the NN-L2H and NN-PL2H approaches manifest lower SSIM medians and higher fluctuations among values.

This analysis confirms that the presence of out-of-domain noise does always affect the computations, but in different ways, and the LIP-CAR approach demonstrates a stable behavior making it a reliable tool when noisy data must be processed. Note that all the regularization terms we use are convex, and our stability comparison analysis accurately reflects the observations made in 3.4 and in Remark 5 specifically.

Finally, in Figure 8, we illustrate the NN-PL2H, LIP-PH2L-TV, and LIP-PH2L-GenTV images computed for the test image 39 at different noise intensities. In the first row, the out-of-domain noise component is null ($\sigma = 0$), and it serves as a reference. For each simulated high-dose image, the figure includes a cropped zoom-in over the tumoral mass. It emerges clearly that while the computed images are quite similar in the in-domain test, the differences among

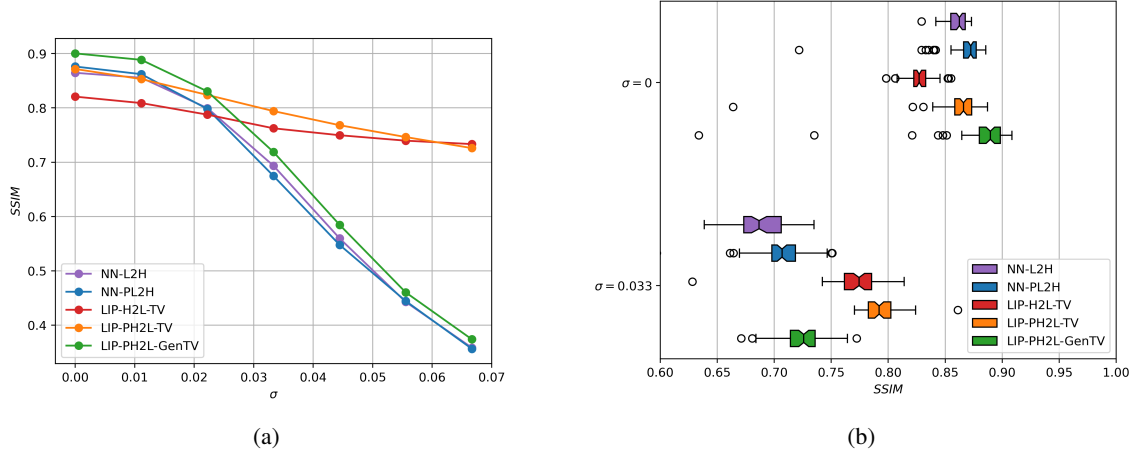


Figure 7: SSIM values on test images, when white Gaussian noise (with standard deviation σ) is added onto the low dose image. (a) SSIM at increasing $\sigma \in [0, 0.066]$ for image 39. (b) Boxplot comparing noiseless results with results obtained by adding noise with standard deviation $\sigma = 0.022$.

the simulated high-dose outputs become more and more evident as σ increases, confirming the different trends of the previous plots. Within the NN-PL2H and the LIP-PH2L-GenTV frameworks, the images are more and more corrupted by a noisy pattern but small and thin details remain almost visible, whereas the TV prior smooths fine details to preserve high contrasts and a high detachability of the main areas of interest. Notably, the shape of the tumoral mass gets altered by the NN-PL2H processing for $\sigma > 0.022$ and almost vanishes for $\sigma = 0.044$.

6 Conclusions

This paper introduces a novel application of neural networks, showing great potential. While many studies have already exploited deep architectures to extract imaging patterns and used them to solve imaging problems with end-to-end approaches directly, we use a convolutional network to learn an operator map in the inverse direction. We then tackle the imaging task as an inverse problem. This approach allows us to handle imaging applications with mathematically grounded tools that belong to the well-established class of optimization and regularization techniques.

As an explanatory application of our approach, we consider a medical challenge involving contrast-agent imaging. The problem, named CAR (Contrast Agent Reduction), consists of digitally simulating the image achieved by injecting the patients with a high dosage of CA medium while subjecting them to a reduced dose (resulting in images with lower contrast and reduced lesion detectability). Despite fast growing interest in the scientific community, the literature on the CAR task from a purely image-to-image approach is still limited. Thus, we have poured our main effort into designing a framework (LIP-CAR) that could be effectively necessary and used in practice. Additionally, as our LIP-CAR proposal solves a regularization model, it does not turn the image processing into a fully unexplainable black box, which is an important feature for medical applications.

We have assessed the LIP-CAR numerical consistency with our mathematical, in-depth theoretical analysis through several experiments on a real, original pre-clinical dataset. Specifically, we have analyzed the predictive accuracy of the simulated images and assessed the LIP-CAR robustness. The quality of the simulated images produced by the LIP-CAR method improves upon or is comparable to those obtained by the state-of-the-art direct approach. Moreover, while direct methods are very sensitive to perturbations, LIP-CAR is stable. The overall LIP-CAR proposal is thus a flexible and well-performing tool for the CAR problem.

To conclude, we highlight that this work represents an introductory study of the LIP-CAR approach. Here, we have not focused on many aspects where it can be further improved. To set some examples, we have not fine-tuned the choice of the optimization formulation in terms of the data-fitting term and, above all, of the regularizer. Even the fine-tuning of the regularization parameter(s) plays an important role in the final results, but this study is out of the scope of this paper.

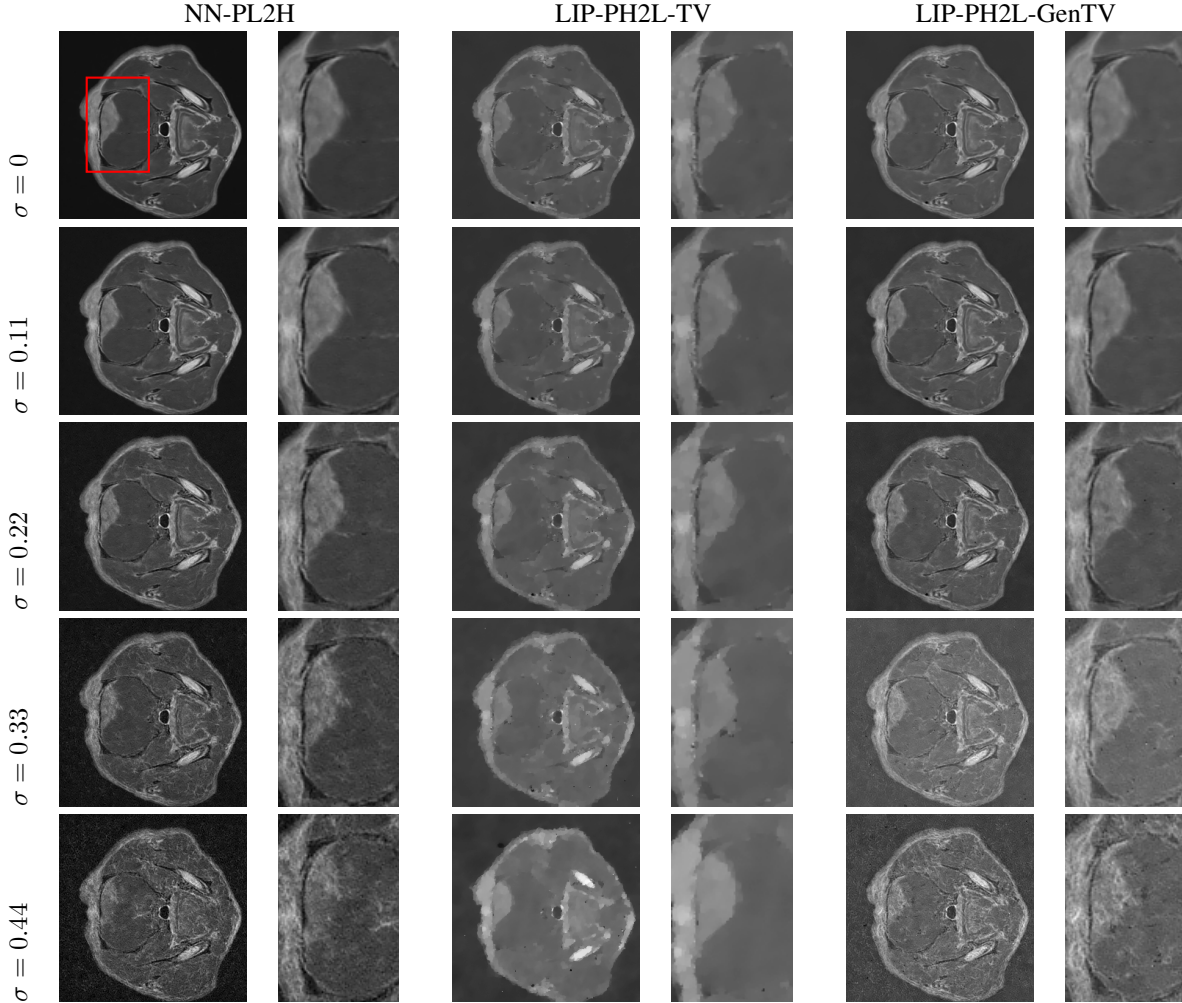


Figure 8: Reconstructed images by NN-PL2H, IP-PH2L-TV, and IP-PH2L-GenTV at varying noise intensities, and the corresponding magnifications on the area depicted by the red rectangle, with the tumoral mass that must be enhanced with the contrast-agent digital simulation.

Acknowledgements

The results presented in this study stem from the DeepCAST project, funded by Bracco Imaging Medical Technologies Co. Ltd.

D. Bianchi is partially supported by the Startup Fund of Sun Yat-sen University.

D. Evangelista and E. Morotti are partially supported by “Gruppo Nazionale per il Calcolo Scientifico (GNCS-INDAM)” (Progetto 2024 “Deep Variational Learning: un approccio combinato per la ricostruzione di immagini”), and the PRIN 2022 project “STILE: Sustainable Tomographic Imaging with Learning and rEgularization”, project code: 20225STXSB, funded by the European Commission under the NextGeneration EU programme.

The authors thank A. Fringuello Mingo and F. La Cava for conducting the MRI preclinical study on a rodent tumour model.

References

- [1] European Medicines Agency - Gadolinium-containing contrast agents - referral. <https://www.ema.europa.eu/en/medicines/human/referrals/gadolinium-containing-contrast-agents>. Accessed: 7 Jul 2024.

- [2] S. Ammari, A. Bône, C. Balleyguier, E. Moulton, É. Chouzenoux, A. Volk, Y. Menu, F. Bidault, F. Nicolas, P. Robert, et al. Can deep learning replace gadolinium in neuro-oncology?: a reader study. *Investigative Radiology*, 57(2):99–107, 2022.
- [3] V. Antun, F. Renna, C. Poon, B. Adcock, and A. C. Hansen. On instabilities of deep learning in image reconstruction and the potential costs of AI. *PNAS*, 117(48):30088–30095, 2020.
- [4] S. Arridge, P. Maass, O. Öktem, and C.-B. Schönlieb. Solving inverse problems using data-driven models. *Acta Numerica*, 28:1–174, 2019.
- [5] D. Bianchi, M. Donatelli, D. Evangelista, W. Li, and E. L. Piccolomini. Graph Laplacian and Neural Networks for Inverse Problems in Imaging: GraphLaNet. In *International Conference on Scale Space and Variational Methods in Computer Vision*, pages 175–186, 2023.
- [6] D. Bianchi, D. Evangelista, S. Aleotti, M. Donatelli, E. L. Piccolomini, and W. Li. A data-dependent regularization method based on the graph laplacian. *arXiv preprint arXiv:2312.16936*, 2023.
- [7] D. Bianchi, G. Lai, and W. Li. Uniformly convex neural networks and non-stationary iterated network Tikhonov (iNETT) method. *Inverse Problems*, 39(5):055002, 2023.
- [8] C. M. Bishop and H. Bishop. *Deep learning: Foundations and concepts*, volume 1. Springer, 2024.
- [9] A. Bône, S. Ammari, J.-P. Lamarque, M. Elhaik, É. Chouzenoux, F. Nicolas, P. Robert, C. Balleyguier, N. Lassau, and M.-M. Rohé. Contrast-enhanced brain MRI synthesis with deep learning: key input modalities and asymptotic performance. In *2021 IEEE 18th International Symposium on Biomedical Imaging (ISBI)*, pages 1159–1163. IEEE, 2021.
- [10] A. Bône, S. Ammari, Y. Menu, C. Balleyguier, E. Moulton, E. Chouzenoux, A. Volk, G. C. Garcia, F. Nicolas, P. Robert, et al. From Dose Reduction to Contrast Maximization: Can Deep Learning Amplify the Impact of Contrast Media on Brain Magnetic Resonance Image Quality? A Reader Study. *Investigative Radiology*, pages 10–1097, 2022.
- [11] W. H. Bush and D. P. Swanson. Acute reactions to intravascular contrast media: types, risk factors, recognition, and specific treatment. *American journal of roentgenology*, 157(6):1153–1161, 1991.
- [12] P. Cascarano, E. L. Piccolomini, E. Morotti, and A. Sebastiani. Plug-and-Play gradient-based denoisers applied to CT image enhancement. *Applied Mathematics and Computation*, 422:126967, 2022.
- [13] C.-W. Cheng, C. Runkel, L. Liu, R. H. Chan, C.-B. Schönlieb, and A. I. Aviles-Rivero. Continuous U-net: Faster, greater and noiseless. *arXiv preprint arXiv:2302.00626*, 2023.
- [14] C. Claussen, M. Laniado, E. Kazner, W. Schörner, and R. Felix. Application of contrast agents in CT and MRI (NMR): their potential in imaging of brain tumors. *Neuroradiology*, 27(2):164–171, 1985.
- [15] M. J. Colbrook, V. Antun, and A. C. Hansen. Can stable and accurate neural networks be computed?—On the barriers of deep learning and Smale’s 18th problem, 2021.
- [16] K. Dabov, A. Foi, V. Katkovnik, and K. Egiazarian. Image denoising by sparse 3-D transform-domain collaborative filtering. *IEEE Transactions on image processing*, 16(8):2080–2095, 2007.
- [17] G. Della Maggiora, C. Castillo-Passi, W. Qiu, S. Liu, C. Milovic, M. Sekino, C. Tejos, S. Uribe, and P. Irarrazaval. DeepSPIO: Super paramagnetic iron oxide particle quantification using deep learning in magnetic resonance imaging. *IEEE Transactions on Pattern Analysis and Machine Intelligence*, 44(1):143–153, 2020.
- [18] H. W. Engl, M. Hanke, and A. Neubauer. *Regularization of inverse problems*. Springer Netherlands, 1996.
- [19] D. Evangelista, E. Morotti, and E. L. Piccolomini. RISING: A new framework for model-based few-view CT image reconstruction with deep learning. *Computerized Medical Imaging and Graphics*, 103:102156, 2023.
- [20] D. Evangelista, E. Morotti, E. L. Piccolomini, and J. Nagy. Ambiguity in solving imaging inverse problems with deep-learning-based operators. *Journal of Imaging*, 9(7):133, 2023.
- [21] M. Genzel, J. Macdonald, and M. März. Solving Inverse Problems With Deep Neural Networks – Robustness Included? *IEEE Transactions on Pattern Analysis and Machine Intelligence*, 45(1):1119–1134, 2023.
- [22] E. Gong, J. M. Pauly, M. Wintermark, and G. Zaharchuk. Deep learning enables reduced gadolinium dose for contrast-enhanced brain MRI. *Journal of magnetic resonance imaging*, 48(2):330–340, 2018.
- [23] I. J. Goodfellow, J. Shlens, and C. Szegedy. Explaining and harnessing adversarial examples. *arXiv preprint arXiv:1412.6572*, 2014.
- [24] N. M. Gottschling, V. Antun, B. Adcock, and A. C. Hansen. The troublesome kernel: why deep learning for inverse problems is typically unstable, 2020.

- [25] R. Haase, T. Pinetz, Z. Bendella, E. Kobler, D. Paech, W. Block, A. Effland, A. Radbruch, and K. Deike-Hofmann. Reduction of gadolinium-based contrast agents in MRI using convolutional neural networks and different input protocols: limited interchangeability of synthesized sequences with original full-dose images despite excellent quantitative performance. *Investigative Radiology*, 58(6):420–430, 2023.
- [26] E. Haber and L. Ruthotto. Stable architectures for deep neural networks. *Inverse problems*, 34(1):014004, 2017.
- [27] P. C. Hansen. *Rank-deficient and discrete ill-posed problems: numerical aspects of linear inversion*. SIAM, 1998.
- [28] J. Haubold, R. Hosch, L. Umutlu, A. Wetter, P. Haubold, A. Radbruch, M. Forsting, F. Nensa, and S. Koitka. Contrast agent dose reduction in computed tomography with deep learning using a conditional generative adversarial network. *Eur. Radiol.*, 31(8):6087–6095, 2021.
- [29] K. Hornik, M. Stinchcombe, and H. White. Multilayer feedforward networks are universal approximators. *Neural networks*, 2(5):359–366, 1989.
- [30] D. P. Kingma and J. Ba. Adam: A method for stochastic optimization. *arXiv preprint arXiv:1412.6980*, 2014.
- [31] H. Li, J. Schwab, S. Antholzer, and M. Haltmeier. NETT: Solving inverse problems with deep neural networks. *Inverse Problems*, 36(6):065005, 2020.
- [32] H. Luo, T. Zhang, N.-J. Gong, J. Tamir, S. P. Venkata, C. Xu, Y. Duan, T. Zhou, F. Zhou, G. Zaharchuk, et al. Deep learning-based methods may minimize GBCA dosage in brain MRI. *European Radiology*, 31(9):6419–6428, 2021.
- [33] S. López-Tapia, R. Molina, and A. K. Katsaggelos. Deep learning approaches to inverse problems in imaging: Past, present and future. *Digital Signal Processing*, 119:103285, 2021.
- [34] J. Menke. Diagnostic accuracy of multidetector CT in acute mesenteric ischemia: systematic review and meta-analysis. *Radiology*, 256(1):93–101, 2010.
- [35] V. Monga, Y. Li, and Y. C. Eldar. Algorithm Unrolling: Interpretable, Efficient Deep Learning for Signal and Image Processing. *IEEE Signal Processing Magazine*, 38(2):18–44, 2021.
- [36] J. Montalt-Tordera, M. Quail, J. A. Steeden, and V. Muthurangu. Reducing contrast agent dose in cardiovascular MR angiography with deep learning. *Journal of Magnetic Resonance Imaging*, 54(3):795–805, 2021.
- [37] E. Morotti, D. Evangelista, and E. Loli Piccolomini. A green prospective for learned post-processing in sparse-view tomographic reconstruction. *Journal of Imaging*, 7(8):139, 2021.
- [38] G. Müller-Franzes, L. Huck, M. Bode, S. Nebelung, C. Kuhl, D. Truhn, and T. Lemainque. Diffusion probabilistic versus generative adversarial models to reduce contrast agent dose in breast MRI. *European Radiology Experimental*, 8(1):53, 2024.
- [39] G. Müller-Franzes, L. Huck, S. Tayebi Arasteh, F. Khader, T. Han, V. Schulz, E. Dethlefsen, J. N. Kather, S. Nebelung, T. Nolte, et al. Using machine learning to reduce the need for contrast agents in breast MRI through synthetic images. *Radiology*, 307(3):e222211, 2023.
- [40] P. Nicod, K. Peterson, M. Levine, H. Dittrich, M. Buchbinder, F. Chappuis, and K. Moser. Pulmonary angiography in severe chronic pulmonary hypertension. *Annals of internal medicine*, 107(4):565–568, 1987.
- [41] S. Pasumarthi, J. I. Tamir, S. Christensen, G. Zaharchuk, T. Zhang, and E. Gong. A generic deep learning model for reduced gadolinium dose in contrast-enhanced brain MRI. *Magn. Reson. Med.*, 86(3):1687–1700, 2021.
- [42] O. Ronneberger, P. Fischer, and T. Brox. U-net: Convolutional networks for biomedical image segmentation. In *Medical Image Computing and Computer-Assisted Intervention—MICCAI 2015: 18th International Conference, Munich, Germany, October 5-9, 2015, Proceedings, Part III 18*, pages 234–241. Springer, 2015.
- [43] D. Ruiz-Balet and E. Zuazua. Neural ODE control for classification, approximation, and transport. *SIAM Review*, 65(3):735–773, 2023.
- [44] V. M. Runge. Critical questions regarding gadolinium deposition in the brain and body after injections of the gadolinium-based contrast agents, safety, and clinical recommendations in consideration of the EMA’s pharmacovigilance and risk assessment committee recommendation for suspension of the marketing authorizations for 4 linear agents. *Investigative radiology*, 52(6):317–323, 2017.
- [45] L. Ruthotto and E. Haber. Deep neural networks motivated by partial differential equations. *Journal of Mathematical Imaging and Vision*, 62(3):352–364, 2020.
- [46] D. Sainz-DeMena, M. Pérez, and J. M. García-Aznar. Exploring the potential of Physics-Informed Neural Networks to extract vascularization data from DCE-MRI in the presence of diffusion. *Medical Engineering & Physics*, 123:104092, 2024.

-
- [47] O. Scherzer, M. Grasmair, H. Grossauer, M. Haltmeier, and F. Lenzen. *Variational methods in imaging*. Springer, 2009.
- [48] J. Schwab, S. Antholzer, and M. Haltmeier. Deep null space learning for inverse problems: convergence analysis and rates. *Inverse Problems*, 35(2):025008, 2019.
- [49] J. Singh and A. Daftary. Iodinated contrast media and their adverse reactions. *Journal of nuclear medicine technology*, 36(2):69–74, 2008.
- [50] X.-C. Tai, H. Liu, and R. Chan. PottsMGNet: A mathematical explanation of encoder-decoder based neural networks. *SIAM Journal on Imaging Sciences*, 17(1):540–594, 2024.
- [51] E. Tjoa and C. Guan. A Survey on Explainable Artificial Intelligence (XAI): Toward Medical XAI. *IEEE Transactions on Neural Networks and Learning Systems*, 32(11):4793–4813, 2021.
- [52] P. S. Tofts, G. Brix, D. L. Buckley, J. L. Evelhoch, E. Henderson, M. V. Knopp, H. B. Larsson, T.-Y. Lee, N. A. Mayr, G. J. Parker, et al. Estimating kinetic parameters from dynamic contrast-enhanced T1-weighted MRI of a diffusible tracer: standardized quantities and symbols. *Journal of Magnetic Resonance Imaging: An Official Journal of the International Society for Magnetic Resonance in Medicine*, 10(3):223–232, 1999.
- [53] A. Vasantachart, Y. Cao, Z. Shen, K. Cheng, M. Gribble, J. Ye, G. Zada, K. Hurth, A. Mathew, S. Guzman, et al. Segmentation and Classification of Grade I and II Meningiomas from Magnetic Resonance Imaging: An Open Annotated Dataset (Meningioma-SEG-CLASS)(Version 1). *Cancer Imaging Arch*, 2023.
- [54] Y. Wang, W. Wu, Y. Yang, H. Hu, S. Yu, X. Dong, F. Chen, and Q. Liu. Deep learning-based 3D MRI contrast-enhanced synthesis from a 2D non contrast T2Flair sequence. *Medical Physics*, 49(7):4478–4493, 2022.
- [55] Z. Wang, A. C. Bovik, H. R. Sheikh, and E. P. Simoncelli. Image quality assessment: from error visibility to structural similarity. *IEEE transactions on image processing*, 13(4):600–612, 2004.
- [56] F. Yang, T.-A. Pham, N. Brandenburg, M. P. Lütolf, J. Ma, and M. Unser. Robust phase unwrapping via deep image prior for quantitative phase imaging. *IEEE Transactions on Image Processing*, 30:7025–7037, 2021.
- [57] D.-X. Zhou. Universality of deep convolutional neural networks. *Applied and computational harmonic analysis*, 48(2):787–794, 2020.
- [58] Z. Zhou and Z.-R. Lu. Gadolinium-based contrast agents for magnetic resonance cancer imaging. *Wiley Interdisciplinary Reviews: Nanomedicine and Nanobiotechnology*, 5(1):1–18, 2013.